crystals

MDPI

Article

$Na_{0.76}V_6O_{15}$@Boron Carbonitride Nanotube Composites as Cathodes for High-Performance Lithium-Ion Capacitors

Deqin Xu [1], Hehe Jiang [2], Zhenyan Liang [1], Zhen Kong [1], Shengfu Liu [1], Lequan Deng [1], Yongliang Shao [1,3,*], Yongzhong Wu [1,3] and Xiaopeng Hao [1,3]

[1] State Key Lab of Crystal Materials, Shandong University, Jinan 250100, China; dqxu@mail.sdu.edu.cn (D.X.); 201712427@mail.sdu.edu.cn (Z.L.); kongzhen@mail.sdu.edu.cn (Z.K.); 201912615@mail.sdu.edu.cn (S.L.); lqdeng@mail.sdu.edu.cn (L.D.); wuyz@sdu.edu.cn (Y.W.); xphao@sdu.edu.cn (X.H.)
[2] Innovative Institute of Chinese Medicine and Pharmacy, Shandong University of Traditional Chinese Medicine, Jinan 250355, China; 60230063@sdutcm.edu.cn
[3] Department of Materials Science and Engineering, Qilu University of Technology (Shandong Academy of Science), Jinan 250353, China
* Correspondence: ylshao@sdu.edu.cn

Abstract: Lithium-ion capacitors (LICs) are considered one of the most promising new-generation energy storage devices because they combine the advantages of lithium-ion batteries and supercapacitors. However, the widely used commercial carbon cathode greatly limits the electrochemical performance of existing LICs due to its limited specific capacity. Improving the specific capacity of the cathode is one of the keys to solving this problem. To this end, the $Na_{0.76}V_6O_{15}$ (NaVO)@boron carbonitride nanotube (BCNNT) cathode has been successfully synthesized via a facile solid phase reaction and hydrothermal reaction followed by annealing. Benefitting from the synergy between the high conductivity of BCNNTs and the high capacity of NaVO, the NaVO@BCN cathode exhibits excellent capacity and good cyclic stability. A LIC was assembled by a prefabricated NaVO@BCN cathode and a prelithiated commercial hard carbon (HC) anode. Notably, the NaVO@BCN−1//HC LIC delivered an energy density of 238.7 Wh kg^{-1} at 200 W kg^{-1} and still delivered 81.9 Wh kg^{-1} even at 20 kW kg^{-1}. Therefore, our strategy provides a novel idea for designing high-performance LICs.

Keywords: $Na_{0.76}V_6O_{15}$@BCN nanotubes; lithium-ion capacitors; cathode; capacitive behavior; Faradaic behavior

Citation: Xu, D.; Jiang, H.; Liang, Z.; Kong, Z.; Liu, S.; Deng, L.; Shao, Y.; Wu, Y.; Hao, X. $Na_{0.76}V_6O_{15}$@Boron Carbonitride Nanotube Composites as Cathodes for High-Performance Lithium-Ion Capacitors. *Crystals* **2022**, *12*, 597. https://doi.org/10.3390/cryst12050597

Academic Editors: Ingo Dierking and Xiaofei Yang

Received: 7 March 2022
Accepted: 21 April 2022
Published: 24 April 2022

1. Introduction

With the transformation of the industrial structure and the change of the energy structure, the demand for reliable and environmentally friendly approaches for energy conversion and storage is becoming more and more urgent, which also presents a huge challenge for electrochemical energy storage devices [1–4]. There are mainly two types of electrochemical energy storage devices: supercapacitors (SCs) and lithium-ion batteries (LIBs) [5]. Due to the Faradaic behavior, i.e., Li ions are injected into or extracted from the electrode materials (cathode or anode) in intercalation/deintercalation or conversion processes [6], LIBs show a high energy density of up to 150–200 Wh kg^{-1} [7] but exhibit inferior power density (<1000 W kg^{-1}) and low cycle stability (<1000 cycles) due to slow diffusion kinetics of lithium ions in the electrode [8]. However, for SCs, a long cycling stability (>10,000 cycles) and superhigh power density exceeding 5 kW kg^{-1} [9] exists due to the process of physical adsorption/desorption of electrolyte ions [10] while unsatisfactory energy density is inevitable. Therefore, lithium-ion capacitors (LICs), which combine the advantages of the two devices, have attracted much attention recently [11].

LICs consist of a capacitive SC-type cathode and Faradaic LIB-type anode with a Li-salt-containing electrolyte [12]. They exhibit enhanced energy density, power density and good cycling stability because of the physical adsorption and desorption process of the

cathode and the diffusion-controlled lithium-ion intercalation and deintercalation process of the anode [6]. However, it is considerably difficult for LICs to demonstrate an ideal energy density, power density and good cycle life because of the kinetic imbalance between the fast adsorption and desorption process of SC-type cathodes and the slow lithium-ion intercalation and deintercalation process of LIB-type anodes [13]. Consequently, it is crucial to design ideal electrode materials to solve this problem. Currently, carbon materials are still the main commercial cathode materials for LICs, for example, graphene, biomass-derived carbons, carbon nanotubes, activated carbon, etc. [14]. Though commercial carbon materials show great rate performance and cycling life, they suffer from an unsatisfactory specific capacity (30–50 mAh g^{-1}) leading to a low energy density [15]. To conquer the problem, strategies of heteroatom doping [6] and compositing with other high energy materials have been developed.

In particular, the boron carbonitride (BCN) ternary system, a new type of two-dimensional material derived from traditional carbon materials, has the advantages of large specific surface area, high specific capacity, abundant active sites, etc. and is a cathode material with great development prospects. In addition, BCN nanotubes (BCNNTs) developed from two-dimensional BCN materials are considered excellent cathode materials for LICs due to the unique hollow tubular structure, which can not only be used as ion transport channels but also as high-quality substrates for preparing composite materials. Compared with traditional carbon nanotubes, the introduction of B and N atoms improves the charge storage capacity of BCN materials. Moreover, the functional groups containing B and N on the carbon surface bring about intercalated pseudocapacitance, different from the double layer capacitance, which enables the electrode to store anions rapidly [16]. In addition, the BCNNTs had been synthesized by a facile solid-phase synthesis approach in our previous report [17] with an enhanced specific capacity and widened voltage window. An energy density of 200 Wh kg^{-1} was provided by the assembled LICs at 239.9 W kg^{-1}. Yu et al. [18] prepared the nitrogen-enriched mesoporous carbon nanospheres/graphene (N-GMCS) composite. The device assembled by the N-GMCS cathode exhibited an energy density of 80 W h kg^{-1} at 152 W kg^{-1} with a satisfactory cycling life (93.1% after 4000 cycles).

Recently, battery-type cathode materials have been developed as cathode materials for LICs. Due to doping metal cations into V_2O_5 layers, vanadate has a higher structural stability and more intercalation sites, attracting extensive attention [19,20]. In particular, sodium vanadate is an excellent cathode material for LIBs because of the high capacity, low cost and great rate performance [21–23]. Composite materials are composed of different materials and, thus, have the advantages of many materials, usually showing superior performance. Therefore, in order to improve the specific capacity of BCNNTs, in this work, a composite cathode material was designed by growing a battery-type cathode material $Na_{0.76}V_6O_{15}$ (NaVO) on the BCNNTs. The NaVO@BCN was prepared by adding BCNNTs to the precursor of NaVO and by using the subsequent hydrothermal method and annealing [24]. The NaVO coated on the surface of the BCNNTs had a rough surface, which could create more active sites to promote the electrochemical reaction. The hollow tubular structure of BCNNTs could be used as an ion transport channel to accelerate ion transport. Benefitting from the synergy between the high conductivity of BCNNTs and the high capacity of the NaVO, the NaVO@BCN showed both good specific capacity and a long cycling life. Compared to the low specific capacity of 37.77 mAh g^{-1} delivered by BCNNTs, the NaVO@BCN-1 could deliver a much higher specific capacity of up to 96.99 mAh g^{-1}. The device fabricated by a NaVO@BCN-1 cathode and prelithiation hard carbon (HC) anode delivered a high energy density of 238.7 Wh kg^{-1} with a satisfactory cycling life (65.5% at 10 A g^{-1} after 5000 cycles). The above results confirmed the feasibility of combining high-capacity battery materials with BCN materials as LIC cathode materials.

2. Materials and Methods

2.1. Material Synthesis

First, 0.45 g boric acid, 6 g urea and 1.5 g polyethylene glycol-2000 (PEG-2000) were added to 40 mL of deionized water, stirred well and dried at 80 °C for 12 h. Then, the obtained precursors were calcinated at 900 °C for 4 h in Ar to prepare BCN nanotubes. Secondly, 0.1781 g sodium dodecyl sulfate and 0.722 g NaCl were added into 0.5 g NH_4VO_3 and BCN nanotubes of different masses (0.5 g, 0.3 g and 0.25 g) for mixed solutions and stirred at 80 °C; then, the mixed solutions were added into a 50 mL autoclave and heated at 200 °C for 12 h. The precursors were obtained by centrifugation and dried at 80 °C in a vacuum overnight. Finally, the NaVO@BCNs were successfully prepared by annealing at 400 °C for 4 h in air. All prepared samples were labeled as NaVO@BCN-1, NaVO@BCN-2 and NaVO@BCN-3, according to the mass percentages of BCNNTs.

2.2. Structure Characterization

X-ray diffraction data of Cu Kα radiation were recorded by an in situ X-ray diffractometer (Rigaku SmartLab, Raleigh, NC, USA). The scanning electron microscope (SEM) images were collected by a field emission scanning electron microscope (FESEM) (Hitachi S-4800, Tokyo, Japan) at 15 kV. The transmission electron microscope (TEM) images were collected by a high-resolution TEM (HRTEM) (JEOL JEM 2100F, Beijing, China) at 200 kV. The Brunauer–Emmett−Teller (BET) method and pore size distribution were used to investigate the specific surface area and pore size distribution, using the Quantachrome Autosorb-IQ gas adsorption analyzer (Quantachrome Autosorb-IQ, Boynton Beach, FL, USA) at 77 K. An in situ confocal Raman spectrometer (Horiba LabRAM HR Evolution, Longrimo, France) was employed to analyze Raman spectroscopy at 532 nm. An X-ray photoelectron spectrometer (Thermo Scientific ESCALAB 250Xi, Sydney, Australia) was used to carry out X-ray photoelectron spectroscopy (XPS) with Al Kα.

2.3. Electrochemical Measurements

Active materials (BCNNTs, NaVO@BCN-1, NaVO@BCN-2 or 3NaVO@BCN-3), polyvinylidene fluoride (PVDF) and conductive carbon black were mixed and added in n-methyl-2-pyrrolidone (NMP) at a mass ratio of 7:1:2 and formed a homogeneous slurry. Then, the obtained slurry was coated on Al foils used as current collectors and dried for 12 h at 80 °C in a vacuum oven to generate the cathode. The anodes of LICs were obtained using 80% commercial hard carbon (HC), 10% carbon black and 10% polyvinylidene fluoride (PVDF) in the same process as the cathode, except for the use of copper foil as the current collector of anode electrodes. All electrodes were loaded with 1–3 mg cm^{-2} active materials and had a diameter of 12 mm. All coin cell (CR2032) assembly steps were operated in a glove box. Li metal was used as the reference electrode and counter electrode to assemble the half cells. The electrolyte used 1 M $LiPF_6$ dissolved in dimethyl carbonate and ethylene carbonate. The LICs were assembled from prelithiated HC anodes and NaVO@BCN-1 or BCN cathodes. The prelithiated procedure was carried out based on our previous works [17]. The mass ratio for the cathode to anode of the NaVO@BCN-1//HC LIC was optimized to be 1:1, which showed the best electrochemical performance.

All tests were performed at 25 °C. The galvanostatic charge/discharge (GCD) test was carried out by using the NEWARE battery measurement system (the testing voltage range of the half-cell anode was 0.01–3 V, and that of the half-cell cathode was 2–4 V). The cyclic voltammetry (CV) measurements were carried out on the CHI660E electrochemical workstation (the testing voltage range of the half-cell anode was 0.01–3 V, the testing voltage range of half-cell cathode was 2–4 V and the testing voltage range of the LIC was 0.01–4 V). The specific capacitance was calculated based on the GCD curves and on the mass of active material for cathodes and anodes. The energy density and power density of LICs were obtained according to the following formula:

$$P = \Delta V \times i/m, \quad (1)$$

$$E = P \times t/3600, \quad (2)$$

$$\Delta V = 1/2\ (Vmax + Vmin), \quad (3)$$

where i was the discharge current (A); m referred to the total mass of active materials, including cathode and anode (kg); t was the discharge time (s); and $Vmax$ and $Vmin$ (V) referred to the discharge initial voltage and discharge end voltage.

3. Results and Discussion

3.1. Morphology and Structure

Figure 1a illustrates the preparation route of the NaVO@BCN. BCNNTs were obtained by calcination and pyrolysis of a mixture of boric acid, urea and polyethylene glycol (PEG) and then added to the precursor of NaVO; the NaVO@BCN was prepared via hydrothermal method and annealing. The morphology of BCN nanotubes and NaVO@BCN samples was tested by SEM. The BCN nanotubes exhibited distinct nanotube structures with an average diameter of ~100 nm, uniformly distributed (Figure 1b). Compared to the BCN nanotubes, the NaVO@BCN-1 showed similar nanotube structures, but the surface of the NaVO@BCN-1 was coated with NaVO, which was rougher, brought in more active sites and promoted the electrochemical reaction (Figure 1c). The hollow tubular structure of BCNNTs could be used as an ion transport channel to accelerate ion transport. Figure S1 (see Supplementary Materials) shows the SEM images of the NaVO@BCN-3 and NaVO@BCN-2. Compared with NaVO@BCN-1, BCNNTs were not completely coated by NaVO due to the lower content of NaVO. As shown in Figure S1a, BCNNTs can be clearly observed, and NaVO is scattered on the surface. With the increase of NaVO content, part of the NaVO was coated on the surface of BCNNTs, but most were still clustered together, which led to low structural stability (Figure S1b). The crystal information and structure of the NaVO@BCN-1 were further analyzed by HR-TEM and selected area electron diffraction (SAED). HR-TEM (Figure 1d) showed a clear plane spacing d = 0.25 nm, which was consistent with the plane (−204) of the monoclinic phase $Na_{0.76}V_6O_{15}$, corresponding to the XRD results. As shown in Figure 2a, NaVO@BCN-1 exhibits two characteristic peaks at about 25° and 42°, corresponding to the planes (002) and (100) for the graphitized structure of BCN nanotubes, respectively [25]. In addition, the NaVO@BCN-1 showed the same diffraction peak as NaVO, corresponding to the monoclinic phase of $Na_{0.76}V_6O_{15}$ (JCPDS Card No. 75-1653) [26]. The SAED pattern was obtained from the HR-TEM image, which indicated the high crystallinity of the NaVO@BCN-1, corresponding to the HR-TEM result. The specific surface area of the BCN nanotubes and NaVO@BCN-1 was investigated by the Brunauer−Emmett−Teller (BET) method, and the pore size was investigated using pore size distribution. The N_2 isothermal adsorption/desorption curve of the NaVO@BCN-1 exhibited a standard type−IV isotherm; there were obvious hysteresis loops in the curve (see Supplementary Materials Figure S2). Two sharp peaks at approximately 4 nm and 18 nm were observed at the pore size distribution curve of inset, indicating that the mesoporous structure was preponderant, which was beneficial to promoting the double-layer reaction and ion transport.

The phase composition of the samples was further analyzed by Raman measurements (Figure 2b). Both of the samples showed two obvious Raman characteristic peaks at about 1350 and 1580 cm^{-1} in D and G bands because of the in-plane stretching vibration of the sp^2 C atom and edge defects. [27]. Compared with the BCN nanotubes, the I_D/I_G of NaVO@BCN-1 increased from 1.09 to 1.16, indicating that higher defect densities and more active sites were beneficial to promoting an electrochemical reaction [28,29]. The oxidation state of the elements and bonding mode in the NaVO@BCN-1 were assessed by XPS. The scan of the NaVO@BCN-1 indicated the presence of Na, V, O, B, C and N elements (Figure 2c). In addition, the six distinct peaks were assigned to Na 1s (1071.45 eV), V 2p (517.3 eV), O 1s (531.9 eV), B 1s (192.3 eV), C 1s (284.55 eV) and N 1s (398.95 eV), respectively. High-resolution XPS spectra of Na 1s, V 2p, O 1s, B 1s, C 1s and N 1s are presented in Figure 2d–i. The high resolution XPS of Na 1s (Figure 2d) showed only one

peak at 1071.45 eV, indicating that the Na element existed only in the form of Na^+ in the NaVO@BCN-1 [30]. As presented in Figure 2e, the vanadium element existed with the oxidation states of +4 and +5 in the NaVO@BCN-1. The four peaks fitted at 515.92, 517.25, 523.82 and 524.86 eV were due to the spin-orbit splitting of $V5^+$ $2p_{3/2}$, $V4^+$ $2p_{3/2}$, $V5^+$ $2p_{1/2}$ and $V4^+$ $2p_{1/2}$ in the NaVO@BCN-1 [31]. The O 1s spectrum (Figure 2f) could be fitted into two peaks located at 531.94 and 529.88 eV. The two peaks were attributed to C−O and V−O bonds, respectively [32,33]. As shown in Figure 2g, the B 1s spectra were fitted into three peaks at 190.58 eV, 191.8 eV and 192.5 eV, indicating that B−C bonds, B−N bonds and B−O bonds coexisted in the NaVO@BCN-1 [34]. Moreover, the C 1s spectrum was deconvoluted into four peaks at 283.93 eV,284.6 eV, 285.9 eV and 288.5 eV, corresponding to the C–B bonds, sp^2 C, C–N bonds and C–O bonds (Figure 2h) [35]. The high content of the sp^2 C ensured that the carbon skeleton played a leading role in the electron transport process. Meanwhile, the spectra of N 1s were fitted into four peaks at 397.9 eV, 398.6 eV, 399.5 eV and 400.2 eV, corresponding to N–B bonds, pyridinic N, pyrrolic N and quaternary N, respectively (Figure 2i) [36]. In particular, the presence of higher pyridinic N introduced more active sites, which improved the electrochemical performance of the materials. Overall, the morphology and structure characterization confirmed that the NaVO@BCN was successfully synthesized.

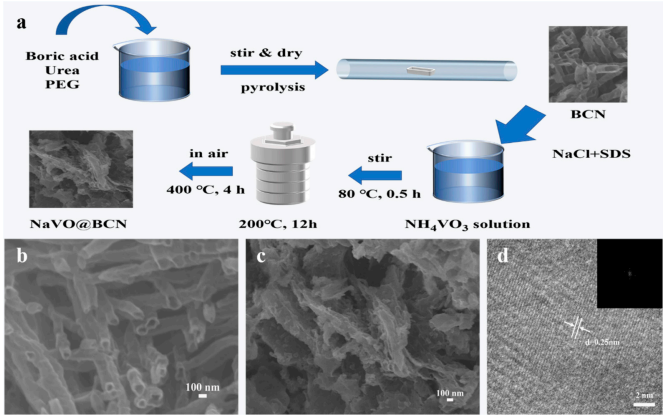

Figure 1. (**a**) Schematic diagram of the preparation of NaVO/BCN composites; (**b**,**c**) SEM images of the BCN nanotubes and NaVO@BCN-1; (**d**) HR-TEM image of the NaVO@BCN-1; inset: the SAED.

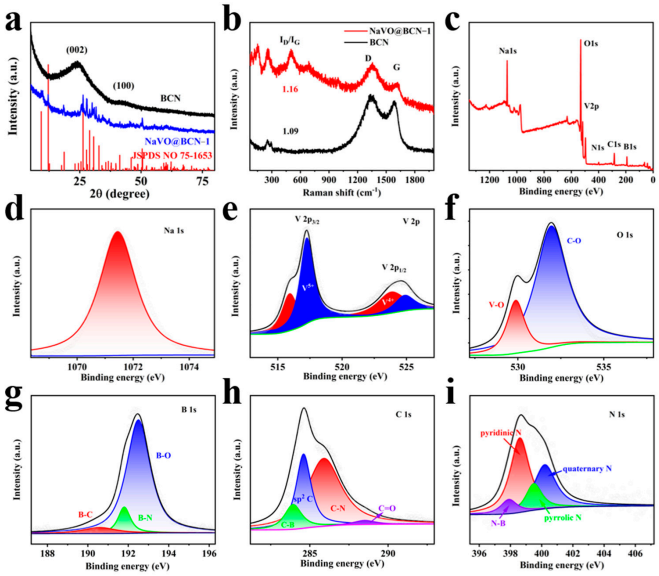

Figure 2. (**a**) XRD patterns of the NaVO@BCN-1 and BCN nanotubes; (**b**) Raman spectra of the NaVO@BCN-1 and BCN nanotubes; (**c**) XPS scan of the NaVO@BCN-1; (**d**–**i**) high-resolution XPS of the NaVO@BCN-1.

3.2. Electrochemical Performance as the Cathode in the Half-Cell

As shown in Figure 3, to investigate the electrochemical behavior of the sample as a LIC cathode, Li foil was used as a reference electrode and counter electrode to assemble half-cells for half-cell tests. The CV curves of the BCN nanotubes and NaVO@BCN cathodes ranging from 2.0 to 4.0 V are shown in Figure 3a. The shape of the CV curve of the BCN nanotubes was approximately rectangular while three obvious reduction peaks appeared in the CV curves of the NaVO@BCN located at around 2.49 V, 2.89 V and 3.26 V, respectively, because of the multistep intercalation of lithium ions [24,37]. The peaks located at 2.49 V and 2.89 V were due to the reduction of vanadium from $V4^+$ to $V3^+$ and $V5^+$ to $V4^+$, respectively, and the peak located at 3.26 V was contributed to the solid solution transformation [24]. The three oxidation peaks located at 2.7 V, 2.96 V and 3.3 V were due to lithium-ion deintercalation. The whole lithium-ion intercalation/deintercalation process can be summarized as follows:

$$Na_{0.76}V_6O_{15} + x\ Li^+ + x\ e^- \leftrightarrow LixNa_{0.76}V_6O_{15}. \quad (4)$$

Moreover, with the increasing NaVO content, the areas of CV curves became larger, indicating a higher capacity due to the increased redox reaction. Figures 3b and S3 (see Supplementary Materials) show the CV curves of the BCN nanotubes and NaVO@BCN. Compared with the CV curves of the other samples, the CV curves of the NaVO@BCN-1 showed the largest area, indicating that the NaVO@BCN-1 had the highest capacity. With the increasing scan rate, the redox peaks moved slightly, and the CV curve remained in good shape, showing quality rate performance and outstanding reaction kinetics. In addition, the CV curves of the NaVO@BCN-1 were approximately rectangular at high current densities, and the redox peaks were not obvious, which demonstrated that capacitance behavior was dominant.

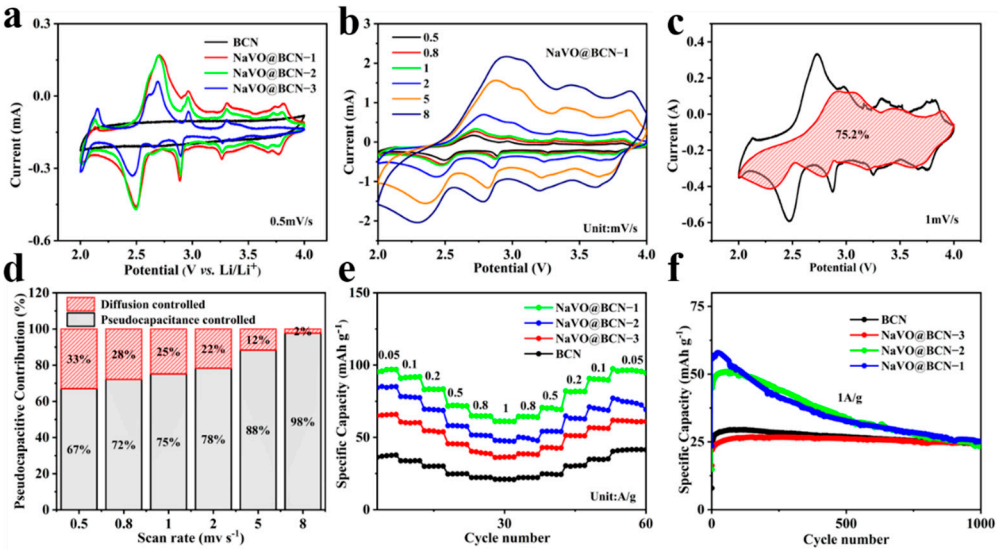

Figure 3. Electrochemical performance of all the samples: (**a**) CV curves of the NaVO@BCN and BCN nanotubes; (**b**) CV curves of the NaVO@BCN-1; (**c**) tThe capacitive contribution (red region) and the total contribution (black line); (**d**) contribution ratio of the capacitive process and the diffusion-controlled Faradaic process of the NaVO@BCN-1; (**e**) the rate performance of the BCN nanotubes and NaVO@BCN; (**f**) cycling stability of the BCN nanotubes and NaVO@BCN at 1 A g^{-1}.

To further analyze the charging and discharging mechanism of the composite cathode, the contribution ratios of the capacitance behavior and diffusion-controlled battery behavior are shown in Figure 3c,d, which were analyzed based on the CV curves of the NaVO@BCN-1 and the following formula:

$$i(V) = k_1 v + k_2 v^{0.5} \quad (5)$$

where i(V) was the measured current at a potential, v was the testing scan rate (mV s^{-1}) and k_1v and $k_2v^{0.5}$ were indicators corresponding to the ratios of capacitive behavior and diffusion-controlled battery behavior, respectively [38–40]. The capacitance contribution curve is shown in Figure 3c at 1 mV s^{-1}, and capacitive contributions account for 75.2% of the total contribution of the NaVO@BCN-1 cathode, which suggests that capacitive behavior is dominant. Moreover, Figure 3d shows the contribution ratios of capacitive process and diffusion-controlled battery process of NaVO@BCN-1. The percentage of capacitance contribution increased from 67% to 98% with the increase of the scanning rate from 0.5, 0.8, 1, 2, 5 to 8 mV s^{-1}, showing that the anion storage of the NaVO@BCN-1 cathode came from both capacitive behavior and diffusion-controlled Faraday behavior. It is remarkable that the NaVO@BCN-1 capacitive behavior dominates at different scan rates, which leads to the excellent rate capability and cycling life.

Figure 3e compares the rate performance of the BCNNTs and NaVO@BCN cathodes in the range of 0.05 to 1 A g^{-1}. Compared with BCNNTs, the NaVO@BCN samples showed a much higher specific capacity. The capacity of the NaVO@BCN was higher than that of the BCNNTs because of the synergistic effect of the high capacity NaVO and high conductivity BCN. For all the NaVO@BCN samples, the NaVO@BCN-1 delivered the highest specific capacity of 96.99 mAh g^{-1} at 0.05 A g^{-1} and a specific capacity of 61.11 mAh g^{-1} at 1 A g^{-1}. In addition, as the current density restored to 0.05 A g^{-1}, the NaVO@BCN-1 still delivered a specific capacity of 95.49 mAh g^{-1}, indicating that the NaVO@BCN-1 cathode had an excellent rate performance. Meanwhile, the NaVO@BCN-1 displayed a decent cycling stability (Figure 3f). The initial capacities of NaVO@BCN at 1 A g^{-1} were 57.94, 50.89 and 29.49 mAh g^{-1}, respectively, higher than the initial capacities of 26.83 mAh g^{-1} for BCN. After 1000 cycles, the NaVO@BCN-1 still exhibited a specific capacity of 25.88 mAh g^{-1}. Compared to the NaVO@BCN-1, the performance of NaVO@BCN-2 and NaVO@BCN-3 were lower, mainly because of their low content of NaVO, which could not completely coat BCNNTs. In summary, these results demonstrate that the NaVO@BCN-1 cathode with combined capacitive behavior and Faradaic behavior is an excellent cathode for high-performance LICs.

3.3. Electrochemical Performances of LICs

The full NaVO@BCN-1//HC LIC was fabricated by a NaVO@BCN-1 cathode and HC anode. The rate performance and cycling stability of the HC anode are shown in Figure S4 (see Supplementary Materials). The HC anode delivered a specific capacity of 177.38 mAh g^{-1} at 0.1 A g^{-1} and 87.86 mAh g^{-1} at 5 A g^{-1}. In addition, as the current density restored to 0.1 A g^{-1}, the HC anode delivered a specific capacity of 243.55 mAh g^{-1} (Figure S4a). Meanwhile, the HC anode displayed a decent cycling stability (Figure S4b,c). The HC anode exhibited an initial capacity of 100.94 and 274.04 mAh g^{-1} at 1 and 0.1 A g^{-1}. However, the HC anode exhibited a higher specific capacity of 184.72 mAh g^{-1} with 1000 cycles and 396.16 mAh g^{-1} with 240 cycles, respectively, which was due to the activation of active materials during the circulation of the charging and discharging process. To obtain the best electrochemical performance, the potential window of the NaVO@BCN-1/HC LIC device was chosen as 0–4.0 V after considering the working potential of the cathode and anode. The CV curves of the NaVO@BCN-1//HC LIC from 8 mV s^{-1} to 100 mV s^{-1} are shown in Figure 4a, and Figure S5a–c shows the CV curves of the other LICs. The CV curves of NaVO@BCN-1// HC LIC were approximately rectangular and have multiple redox peaks, indicating that a synergistic mechanism occurred in the device. During the charging process, the NaVO@BCN-1 cathode absorbed a large number of $PF6^-$ ions (capacitive behavior) while Li^+ were embedded in the HC anode (battery behavior). Moreover, the oxidation of vanadium ions in the NaVO (battery behavior) also increased the energy density [18,33]. The reverse process occurred during discharging. As the scan rate increased, the CV curve of the NaVO@BCN-1 hardly changed, indicating excellent rate performance and reversibility. Figure 4b and Figure S5d,f (see Supplementary Materials) show the GCD curves of the NaVO@BCN-1//HC LIC and other devices. Compared with

the GCD curves of other devices, the GCD curves of the NaVO@BCN-1//HC LIC showed the largest area, indicating that the NaVO@BCN-1 had the highest capacity. The nonlinear shape of the GCD curves of the NaVO@BCN-1//HC LIC showed the "synergistic effect" of the capacitive behavior and battery behavior, corresponding to the CV curve above. In addition, the symmetrical shape of GCD curves also indicated an excellent coulombic efficiency and reversibility.

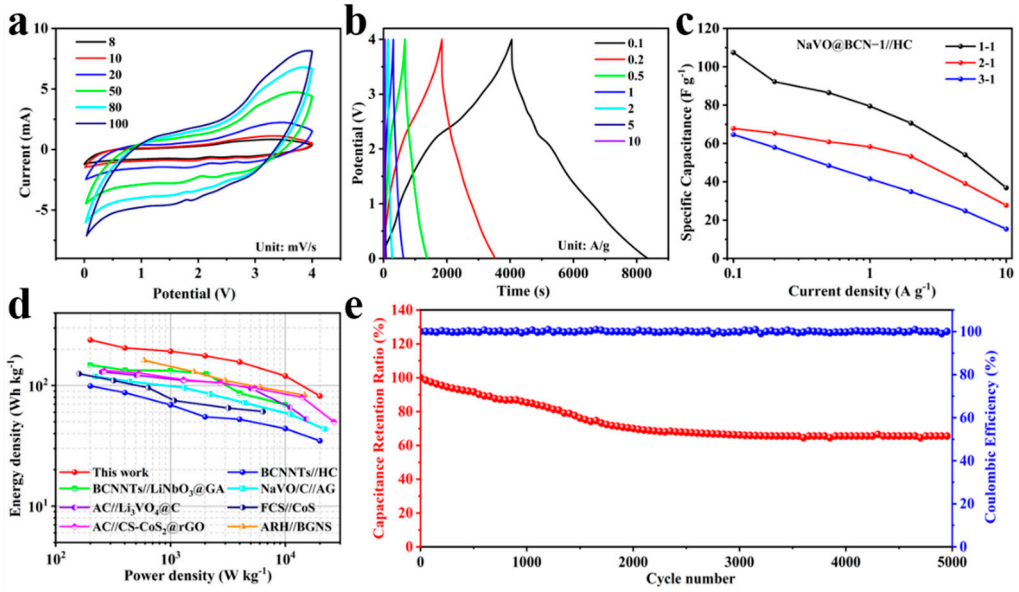

Figure 4. (**a**) CV curves of the NaVO@BCN-1//HC LIC; (**b**) GCD curves of the NaVO@BCN-1//HC LIC; (**c**) specific capacitance of the LICs with different cathode and anode mass ratios; (**d**) Ragone plots of the NaVO@BCN-1//HC LIC and other advanced LICs in previous work; (**e**) cycling performance of the NaVO@BCN-1//HC LIC from 0–4 V at 10 A g^{-1}.

The capacity balance of the cathode and anode is crucial to improving the electrochemical performance of LICs [41]. Therefore, three cases with the mass load ratios of cathode and anode of 1:1–3:1 were studied. The specific capacities of different cathode and anode mass ratios were calculated based on the GCD curves and Formulas (1)–(3). The LICs with cathode and anode mass ratios of 1:1 showed the highest specific capacity (Figure 4c), with a specific capacity of 107.43 F g^{-1} at a current density of 0.1 A g^{-1} and a specific capacity of 36.88 F g^{-1} even at 10 A g^{-1}. However, the specific capacity of LICs with cathode and anode mass ratios of 3:1 was only 64.62 F g^{-1} at 0.1 A g^{-1} and 15.35 F g^{-1} at 10 A g^{-1}, respectively. Compared with the BCN//HC LIC and several previously reported devices, the NaVO@BCN-1//HC LIC showed better performance using Ragone plots (Figure 4d) [15,26,42–45]. According to the GCD curves and Formulas (1)–(3), the energy density and power density of the LICs were also obtained. The NaVO@BCN-1// HC LIC delivered a high energy density of 238.7 Wh kg^{-1} at a power density of 200 W kg^{-1} and could still deliver 81.9 Wh kg^{-1} even at 20 kW kg^{-1}, which showed an excellent rate performance. Moreover, the NaVO@BCN-1//HC LIC exhibited a better electrochemical performance than some LICs in similar studies (see Supplementary Materials Table S1), for example, the BCNNTs//$LiNbO_3$@GA [42], AC//V_2O_5@CNT [46], NS-DPC//$Ti_3C_2T_x$@Fe_2O_3 [47], LMO-MSs@GNSs//AC [48] and $Li_3V_2(PO_4)_3$/C//AC [49]. Moreover, the NaVO@BCN-1//HC LIC retained a capacitance retention ratio of 65.5% at 10 A g^{-1} after 5000 cycles, exhibiting good cycling stability (Figure 4e).

4. Conclusions

In this work, the NaVO@BCN was prepared by a facile hydrothermal method and annealing to improve the specific capacity of BCN nanotubes as a cathode material for LICs. The surface of the NaVO grown on BCN nanotubes is very rough, which can create

more active sites to promote the electrochemical reaction. The hollow tubular structure of BCN nanotubes can be used as an ion transport channel to accelerate ion transport. Due to the synergy between the high capacity of the NaVO and the high conductivity of the BCN, the NaVO@BCN-1 shows excellent electrochemical performances. The NaVO@BCN-1 exhibits a high specific capacity of 96.99 mAh g^{-1}. The assembled NaVO@BCN-1//HC LIC delivers a high energy density of 238.7 Wh kg^{-1} at 200 W kg^{-1} and an energy density of 81.9 Wh kg^{-1} even at 20 kW kg^{-1} with a satisfactory cycling life (65.5% at 10 A g^{-1} after 5000 cycles). In summary, it is feasible to prepare advanced LICs by using composite cathodes composed of BCN and high-capacity battery materials.

Supplementary Materials: The following supporting information can be downloaded at https://www.mdpi.com/article/10.3390/cryst12050597/s1. Figure S1: SEM imges of NaVO@BCN-3 and NaVO@BCN-2; Figure S2: nitrogen adsorption/desorption isotherms of NaVO@BCN-1 and BCN. Inset: the pore size distributions.; Figure S3: CV curves of BCN nanotubes and NaVO@BCN; Figure S4: rate and cycling performance of HC; Figure S5: electrochemical performances of the LICs. Table S1. Electrochemical performance of different cathode electrodes and the relevant LICs.

Author Contributions: Conceptualization, Y.W. and X.H.; methodology, H.J., Z.K. and Y.S.; validation, S.L., L.D. and Z.L.; investigation, D.X.; project administration, Y.S.; writing—original draft, D.X.; writing—editing and review, D.X., H.J., Y.W. and X.H. All authors have read and agreed to the published version of the manuscript.

Funding: This research was funded by [National Natural Science Foundation of China] grant number [No. 51872162, 11890700]. And the APC was funded by [Yongliang Shao].

Data Availability Statement: Not applicable.

Acknowledgments: This work was supported by National Natural Science Foundation of China (Contract No. 51872162, 11890700) and Key R&D Innovation Program of Shandong Province—Major Innovation Project (2019TSLH0116).

Conflicts of Interest: The authors declare no conflict of interest.

References

1. Chu, S.; Majumdar, A. Opportunities and challenges for a sustainable energy future. *Nature* **2012**, *488*, 294–303. [CrossRef]
2. Chu, S.; Cui, Y.; Liu, N. The path towards sustainable energy. *Nat. Mater.* **2016**, *16*, 16–22. [CrossRef]
3. Bonaccorso, F.; Colombo, L.; Yu, G.; Stoller, M.; Tozzini, V.; Ferrari, A.C.; Ruoff, R.S.; Pellegrini, V. 2D materials. Graphene, related two-dimensional crystals, and hybrid systems for energy conversion and storage. *Science* **2015**, *347*, 1246501. [CrossRef]
4. Goodenough, J.B. Energy storage materials: A perspective. *Energy Storage Mater.* **2015**, *1*, 158–161. [CrossRef]
5. Liu, S.; Shi, D.; Tu, H.; Yao, X.; Deng, L.; Xu, D.; Shao, Y.; Wu, Y.; Hao, X. Self-Supported Fluorine-Doped Boron Carbonitride Porous Aerogels for High-Performance Supercapacitors. *Energy Technol.* **2021**, *9*, 2100824. [CrossRef]
6. Jin, L.; Shen, C.; Shellikeri, A.; Wu, Q.; Zheng, J.; Andrei, P.; Zhang, J.-G.; Zheng, J.P. Progress and perspectives on pre-lithiation technologies for lithium ion capacitors. *Energy Environ. Sci.* **2020**, *13*, 2341–2362. [CrossRef]
7. Zou, K.; Cai, P.; Cao, X.; Zou, G.; Hou, H.; Ji, X. Carbon materials for high-performance lithium-ion capacitor. *Curr. Opin. Electrochem.* **2020**, *21*, 31–39. [CrossRef]
8. Wang, H.; Zhu, C.; Chao, D.; Yan, Q.; Fan, H.J. Nonaqueous Hybrid Lithium-Ion and Sodium-Ion Capacitors. *Adv. Mater.* **2017**, *29*, 1702093. [CrossRef]
9. Li, B.; Zheng, J.; Zhang, H.; Jin, L.; Yang, D.; Lv, H.; Shen, C.; Shellikeri, A.; Zheng, Y.; Gong, R.; et al. Electrode Materials, Electrolytes, and Challenges in Nonaqueous Lithium-Ion Capacitors. *Adv. Mater.* **2018**, *30*, e1705670. [CrossRef]
10. Wang, Y.K.; Liu, M.C.; Cao, J.; Zhang, H.J.; Kong, L.B.; Trudgeon, D.P.; Li, X.; Walsh, F.C. 3D Hierarchically Structured CoS Nanosheets: Li (+) Storage Mechanism and Application of the High-Performance Lithium-Ion Capacitors. *ACS Appl. Mater. Interfaces* **2020**, *12*, 3709–3718. [CrossRef]
11. Han, P.; Xu, G.; Han, X.; Zhao, J.; Zhou, X.; Cui, G. Lithium Ion Capacitors in Organic Electrolyte System: Scientific Problems, Material Development, and Key Technologies. *Adv. Energy Mater.* **2018**, *8*, 1801243. [CrossRef]
12. Jin, L.; Yuan, J.; Shellikeri, A.; Naderi, R.; Qin, N.; Lu, Y.; Fan, R.; Wu, Q.; Zheng, J.; Zhang, C.; et al. An Overview on Design Parameters of Practical Lithium-Ion Capacitors. *Batter. Supercaps* **2021**, *4*, 749–757. [CrossRef]
13. Sui, D.; Wu, M.; Liu, Y.; Yang, Y.; Zhang, H.; Ma, Y.; Zhang, L.; Chen, Y. High performance Li-ion capacitor fabricated with dual graphene-based materials. *Nanotechnology* **2021**, *32*, 015403. [CrossRef] [PubMed]
14. Sui, D.; Chang, M.; Peng, Z.; Li, C.; He, X.; Yang, Y.; Liu, Y.; Lu, Y. Graphene-Based Cathode Materials for Lithium-Ion Capacitors: A Review. *Nanomaterials* **2021**, *11*, 2771. [CrossRef]

15. Liang, Z.; Tu, H.; Shi, D.; Chen, F.; Jiang, H.; Shao, Y.; Wu, Y.; Hao, X. In Situ Growing BCN Nanotubes on Carbon Fibers for Novel High-Temperature Supercapacitor with Excellent Cycling Performance. *Small* **2021**, *17*, e2102899. [CrossRef]
16. Xia, Q.; Yang, H.; Wang, M.; Yang, M.; Guo, Q.; Wan, L.; Xia, H.; Yu, Y. High Energy and High Power Lithium-Ion Capacitors Based on Boron and Nitrogen Dual-Doped 3D Carbon Nanofibers as Both Cathode and Anode. *Adv. Energy Mater.* **2017**, *7*, 1701336. [CrossRef]
17. Jiang, H.; Shi, D.; Sun, X.; Wang, S.; Li, Y.; Chang, B.; Zhang, B.; Shao, Y.; Wu, Y.; Hao, X. Boron Carbonitride Lithium-Ion Capacitors with an Electrostatically Expanded Operating Voltage Window. *ACS Appl. Mater. Interfaces* **2020**, *12*, 47425–47434. [CrossRef]
18. Yu, X.; Zhan, C.; Lv, R.; Bai, Y.; Lin, Y.; Huang, Z.; Shen, W.; Qiu, X.; Kang, F. Ultrahigh-rate and high-density lithium-ion capacitors through hybriding nitrogen-enriched hierarchical porous carbon cathode with prelithiated microcrystalline graphite anode. *Nano Energy* **2015**, *15*, 43–53. [CrossRef]
19. Pan, A.; Zhang, J.; Cao, G.; Liang, S.; Wang, C.; Nie, Z.; Arey, B.W.; Xu, W.; Liu, D.; Xiao, J.; et al. Nanosheet-structured LiV_3O_8 with high capacity and excellent stability for high energy lithium batteries. *J. Mater. Chem.* **2011**, *21*, 10077. [CrossRef]
20. Bach, S.; Boudaoud, A.; Emery, N.; Baddour-Hadjean, R.; Pereira-Ramos, J.P. $K_{0.5}V_2O_5$: A novel Li intercalation compound as positive electrode material for rechargeable lithium batteries. *Electrochim. Acta* **2014**, *119*, 38–42. [CrossRef]
21. Tang, Y.; Sun, D.; Wang, H.; Huang, X.; Zhang, H.; Liu, S.; Liu, Y. Synthesis and electrochemical properties of NaV_3O_8 nanoflakes as high-performance cathode for Li-ion battery. *RSC Adv.* **2014**, *4*, 8328. [CrossRef]
22. Lu, Y.; Wu, J.; Liu, J.; Lei, M.; Tang, S.; Lu, P.; Yang, L.; Yang, H.; Yang, Q. Facile Synthesis of $Na_{0.33}V_2O_5$ Nanosheet-Graphene Hybrids as Ultrahigh Performance Cathode Materials for Lithium Ion Batteries. *ACS Appl. Mater. Interfaces* **2015**, *7*, 17433–17440. [CrossRef] [PubMed]
23. Ko, Y.W.; Teh, P.F.; Pramana, S.S.; Wong, C.L.; Su, T.; Li, L.; Madhavi, S. Electrospun Single-Phase $Na_{1.2}V_3O_8$ Materials with Tunable Morphologies as Cathodes for Rechargeable Lithium-Ion Batteries. *ChemElectroChem* **2015**, *2*, 837–846. [CrossRef]
24. Yang, K.; Fang, G.; Zhou, J.; Qin, M.; Tang, Y.; Pan, A.; Liang, S. Hydrothermal synthesis of sodium vanadate nanobelts as high-performance cathode materials for lithium batteries. *J. Power Sources* **2016**, *325*, 383–390. [CrossRef]
25. Yang, M.; Shi, D.; Sun, X.; Li, Y.; Liang, Z.; Zhang, L.; Shao, Y.; Wu, Y.; Hao, X. Shuttle confinement of lithium polysulfides in borocarbonitride nanotubes with enhanced performance for lithium–sulfur batteries. *J. Mater. Chem. A* **2020**, *8*, 296–304. [CrossRef]
26. Lu, R.; Ren, X.; Wang, C.; Zhan, C.; Nan, D.; Lv, R.; Shen, W.; Kang, F.; Huang, Z.H. $Na_{0.76}V_6O_{15}$/Activated Carbon Hybrid Cathode for High-Performance Lithium-Ion Capacitors. *Materials* **2021**, *14*, 122. [CrossRef]
27. Chang, B.; Li, L.; Shi, D.; Jiang, H.; Ai, Z.; Wang, S.; Shao, Y.; Shen, J.; Wu, Y.; Li, Y.; et al. Metal-free boron carbonitride with tunable boron Lewis acid sites for enhanced nitrogen electroreduction to ammonia. *Appl. Catal. B Environ.* **2021**, *283*, 119622. [CrossRef]
28. Dong, Y.; Xu, J.; Chen, M.; Guo, Y.; Zhou, G.; Li, N.; Zhou, S.; Wong, C.-P. Self-assembled NaV_6O_{15} flower-like microstructures for high-capacity and long-life sodium-ion battery cathode. *Nano Energy* **2020**, *68*, 104357. [CrossRef]
29. Baddour-Hadjean, R.; Bach, S.; Emery, N.; Pereira-Ramos, J.P. The peculiar structural behaviour of β-$Na_{0.33}V_2O_5$ upon electrochemical lithium insertion. *J. Mater. Chem.* **2011**, *21*, 11296–11305. [CrossRef]
30. Luo, C.; Xiao, L.; Wu, X. Aqueous zinc ion batteries based on sodium vanadate electrode materials with long lifespan and high energy density. *Mater. Adv.* **2022**, *3*, 604–610. [CrossRef]
31. Xu, X.; Chang, S.; Zeng, T.; Luo, Y.; Fang, D.; Xie, M.; Yi, J. Synthesis of $CeVO_4$-V_2O_5 nanowires by cation-exchange method for high-performance lithium-ion battery electrode. *J. Alloy. Compd.* **2021**, *887*, 161237. [CrossRef]
32. Lu, J.; Zhang, D.; Wang, Y.; Ni, S. Na_3VO_4 as a new anode material for lithium-ion batteries. *New J. Chem.* **2021**, *45*, 11506–11511. [CrossRef]
33. Shi, D.; Chang, B.; Ai, Z.; Jiang, H.; Chen, F.; Shao, Y.; Shen, J.; Wu, Y.; Hao, X. Boron carbonitride with tunable B/N Lewis acid/base sites for enhanced electrocatalytic overall water splitting. *Nanoscale* **2021**, *13*, 2849–2854. [CrossRef] [PubMed]
34. Tabassum, H.; Zou, R.; Mahmood, A.; Liang, Z.; Guo, S. A catalyst-free synthesis of B, N co-doped graphene nanostructures with tunable dimensions as highly efficient metal free dual electrocatalysts. *J. Mater. Chem. A* **2016**, *4*, 16469–16475. [CrossRef]
35. Florent, M.; Bandosz, T.J. Irreversible water mediated transformation of BCN from a 3D highly porous form to its nonporous hydrolyzed counterpart. *J. Mater. Chem. A* **2018**, *6*, 3510–3521. [CrossRef]
36. Shi, D.; Yang, M.; Zhang, B.; Ai, Z.; Hu, H.; Shao, Y.; Shen, J.; Wu, Y.; Hao, X. BCN-Assisted Built-In Electric Field in Heterostructure: An Innovative Path for Broadening the Voltage Window of Aqueous Supercapacitor. *Adv. Funct. Mater.* **2021**, *32*, 2108843. [CrossRef]
37. Yan, M.; Zhao, L.; Zhao, K.; Wei, Q.; An, Q.; Zhang, G.; Wei, X.; Ren, W.; Mai, L. The Capturing of Ionized Oxygen in Sodium Vanadium Oxide Nanorods Cathodes under Operando Conditions. *Adv. Funct. Mater.* **2016**, *26*, 6555–6562. [CrossRef]
38. Chen, L.; Chen, L.; Zhai, W.; Li, D.; Lin, Y.; Guo, S.; Feng, J.; Zhang, L.; Song, L.; Si, P.; et al. Tunable synthesis of Li_xMnO_2 nanowires for aqueous Li-ion hybrid supercapacitor with high rate capability and ultra-long cycle life. *J. Power Sources* **2019**, *413*, 302–309. [CrossRef]
39. Cui, Y.; Liu, W.; Lyu, Y.; Zhang, Y.; Wang, H.; Liu, Y.; Li, D. All-carbon lithium capacitor based on salt crystal-templated, N-doped porous carbon electrodes with superior energy storage. *J. Mater. Chem. A* **2018**, *6*, 18276–18285. [CrossRef]
40. Augustyn, V.; Simon, P.; Dunn, B. Pseudocapacitive oxide materials for high-rate electrochemical energy storage. *Energy Environ. Sci.* **2014**, *7*, 1597–1614. [CrossRef]

41. Feng, J.; Chernova, N.A.; Omenya, F.; Tong, L.; Rastogi, A.C.; Stanley Whittingham, M. Effect of electrode charge balance on the energy storage performance of hybrid supercapacitor cells based on $LiFePO_4$ as Li-ion battery electrode and activated carbon. *J. Solid State Electrochem.* **2017**, *22*, 1063–1078. [CrossRef]
42. Jiang, H.; Wang, S.; Zhang, B.; Shao, Y.; Wu, Y.; Zhao, H.; Lei, Y.; Hao, X. High performance lithium-ion capacitors based on $LiNbO_3$-arched 3D graphene aerogel anode and BCNNT cathode with enhanced kinetics match. *Chem. Eng. J.* **2020**, *396*, 125207. [CrossRef]
43. Ren, X.; Ai, D.; Zhan, C.; Lv, R.; Kang, F.; Huang, Z.-H. 3D porous Li_3VO_4@C composite anodes with ultra-high rate capacity for lithium-ion capacitors. *Electrochim. Acta* **2020**, *355*, 136819. [CrossRef]
44. Bhattacharjee, U.; Bhowmik, S.; Ghosh, S.; Vangapally, N.; Martha, S.K. Boron-doped graphene anode coupled with microporous activated carbon cathode for lithium-ion ultracapacitors. *Chem. Eng. J.* **2022**, *430*, 132835. [CrossRef]
45. Shang, Y.; Sun, X.; Chen, Z.; Xiong, K.; Zhou, Y.; Cai, S.; Zheng, C. Carbon-doped surface unsaturated sulfur enriched CoS_2@rGO aerogel pseudocapacitive anode and biomass-derived porous carbon cathode for advanced lithium-ion capacitors. *Front. Chem. Sci. Eng.* **2021**, *15*, 1500–1513. [CrossRef]
46. Ren, J.J.; Su, L.W.; Qin, X.; Yang, M.; Wei, J.P.; Zhou, Z.; Shen, P.W. Pre-lithiated graphene nanosheets as negative electrode materials for Li-ion capacitors with high power and energy density. *J. Power Sources* **2014**, *264*, 108–113. [CrossRef]
47. Tang, X.; Liu, H.; Guo, X.; Wang, S.; Wu, W.; Mondal, A.K.; Wang, C.; Wang, G. A novel lithium-ion hybrid capacitor based on an aerogel-like MXene wrapped Fe_2O_3 nanosphere anode and a 3D nitrogen sulphur dual-doped porous carbon cathode. *Mat. Chem. Front.* **2018**, *2*, 1811–1821. [CrossRef]
48. Li, J.; Zhang, X.; Peng, R.; Huang, Y.; Guo, L.; Qi, Y. $LiMn_2O_4$/graphene composites as cathodes with enhanced electrochemical performance for lithium-ion capacitors. *RSC Adv.* **2016**, *6*, 54866–54873. [CrossRef]
49. Zhuang, B.; Wu, Z.; Chu, W.; Gao, Y.; Cao, Z.; Bold, T.; Yang, N. High-Performance Lithium-ion Supercapatteries Constructed Using $Li_3V_2(PO_4)_3$/C Mesoporous Nanosheets. *ChemistrySelect* **2019**, *4*, 9822–9828. [CrossRef]